

THE DYNAMICAL M/L -PROFILE AND DISTANCE OF THE GLOBULAR CLUSTER M15.¹

REMCO VAN DEN BOSCH², TIM DE ZEEUW², KARL GEBHARDT³,
EVA NOYOLA³, GLENN VAN DE VEN²

(Received; Revised; Accepted)
ApJ, accepted for publication

ABSTRACT

We construct orbit-based axisymmetric dynamical models for the globular cluster M15 which fit groundbased line-of-sight velocities and Hubble Space Telescope line-of-sight velocities and proper motions. This allows us to constrain the variation of the mass-to-light ratio M/L as a function of radius in the cluster, and to measure the distance and inclination of the cluster. We obtain a best-fitting inclination of $60^\circ \pm 15^\circ$, a dynamical distance of 10.3 ± 0.4 kpc and an M/L profile with a central peak. The inferred mass in the central 0.05 parsec is $3400 M_\odot$, implying a central density of at least $7.4 \times 10^6 M_\odot \text{pc}^{-3}$. We cannot distinguish the nature of the central mass concentration. It could be an IMBH or it could be large number of compact objects, or it could be a combination. The central 4 arcsec of M15 appears to contain a rapidly spinning core, and we speculate on its origin.

Subject headings: distance scale — globular clusters: individual (M15) — stellar dynamics — stars: kinematics — black hole physics

1. INTRODUCTION

M15 is a well-studied globular cluster. It has a very steep central luminosity profile, and may be in the post-core-collapse stage (e.g., Phinney 1993; Trager, King & Djorgovski 1995). Measurements of nearly two thousand line-of-sight velocities (from the ground and with HST) and proper motions (with HST) have recently become available (Gebhardt et al. 2000, hereafter G00; McNamara, Harrison & Anderson 2003, hereafter M03).

McNamara, Harrison & Baumgardt (2004, hereafter M04) restricted themselves to the subset of 237 stars inside 0.3 of the center of M15 for which both Fabry–Perot radial velocities and HST proper motions were measured, and computed the mean dispersions in these measurements. Assuming the cluster is an isotropic sphere, and the observed stars are representative, the ratio of these dispersions (one in km s^{-1} , the other in mas yr^{-1}) provides the distance (Cudworth 1979, Binney & Tremaine 1987). M04 find a distance of 9.98 ± 0.47 kpc, which is consistent with the canonical value of 10.4 kpc (Durrell & Harris 1993), but is smaller than, e.g., the recent determination of 11.2 kpc by Kraft & Ivans (2003) who used a globular cluster metallicity scale, based upon Fe II lines.

Here we extend the M04 study by using a larger fraction of the line-of-sight velocity and proper motion samples, and comparing these with more general dynamical models to study the internal structure of the cluster as a function of radius. We follow the approach taken by van de Ven et al. (2005, hereafter V05), who constructed axisymmetric dynamical models for the globular cluster ω Centauri and fitted these to groundbased proper motions and line-of-sight velocities. This technique provides the internal dynamical structure as well as the inclination of the cluster, an unbiased and accurate dynamical distance, and the M/L -profile. Our aim is to derive

similar information for M15. We are particularly interested in the M/L profile, as significant mass segregation is believed to have occurred in the cluster (Dull et al. 1997). The HST proper motions have sufficient spatial resolution to study the dynamical structure and mass concentration in the center.

In Section 2, we summarize the observational data. In Section 3, we consider the influence of measurement errors on the data, select the stars to be used for the dynamical modeling and also study the possible residual systematic effects in the observed mean motions. We construct dynamical models in Section 4, derive a distance, and investigate the effect of the unknown inclination and of radial M/L variations in the cluster. We discuss the dynamics of the central 0.2 parsec of M15 in Section 5, and summarize our conclusions in Section 6.

2. OBSERVATIONAL DATA

We discuss, in turn, the surface brightness distribution, the line-of-sight velocities, and the proper motion data for M15.

2.1. Surface brightness distribution

The surface brightness distribution of M15 has been studied in detail by a number of authors (Lauer et al. 1991; Trager et al. 1995; Guhathakurta et al. 1996; Sosin & King 1997). Noyola & Gebhardt (2005) reanalysed archival WFPC2 images with a new technique which measures the integrated light to determine the surface-brightness distribution in the dense central regions of the cluster. They combined this with the groundbased profile from Trager et al. (1995). The surface-brightness profile is a power-law in the inner arcsecond, with slope -0.62 ± 0.06 , which agrees with the determinations by Guhathakurta et al. (1996) and Sosin & King (1997).

Because the surface-brightness distribution of M15 is only slightly flattened and the individual stars in the cluster are resolved, it is difficult to estimate the ellipticity and the position angle (PA) of the major axis. Guhathakurta et al. (1996) measured an average ellipticity of $\epsilon = 0.05 \pm 0.04$. Determinations of the PA of the photometric major axis as measured from North through East vary from 125° (White & Shawl 1987) to 45° (from a DSS image) at large radii, and is given as $60^\circ \pm 20^\circ$ by Guhathakurta et al. (1996). Gebhardt et al.

Electronic address: bosch@strw.leidenuniv.nl

¹ Based on observations with the NASA/ESA Hubble Space Telescope obtained at the Space Telescope Science Institute, which is operated by the Association of Universities for Research in Astronomy, Incorporated, under NASA contract NAS5-26555.

² Sterrewacht Leiden, Postbus 9513, 2300 RA Leiden, The Netherlands.

³ Astronomy Department, University of Texas, Austin.

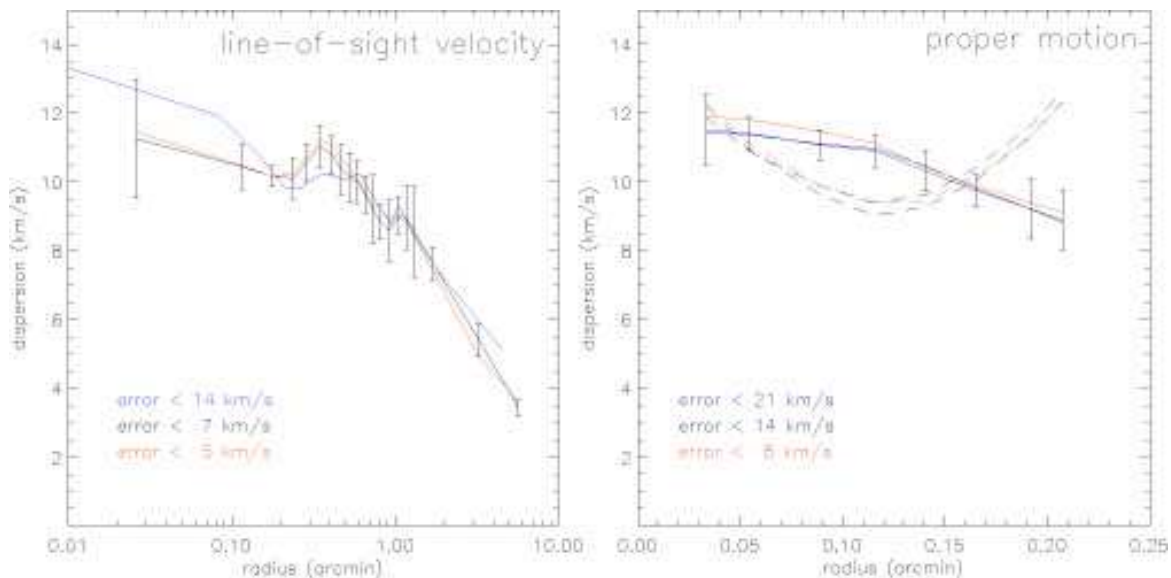


FIG. 1.— Smoothed radial dispersion profiles of the line-of-sight velocities and proper motions for various cuts in the velocity error distribution. a) Line-of-sight velocities. Red is an uncertainty cut of 5 km s^{-1} or less, black is for 7 km s^{-1} , and blue is for 14 km s^{-1} . Uncertainty cuts below 5 km s^{-1} show no difference from the red lines. Every error bar represents a radial ring containing 60 stars. b) major (solid lines) and minor (dashed lines) axis proper motions for various cuts in the velocity error distribution. Red is an uncertainty cut of 8 km s^{-1} or less, black is for 14 km s^{-1} , and blue is for 21 km s^{-1} (for an assumed distance of 10 kpc). Uncertainty cuts below 8 km s^{-1} show no difference from the red curves. Every error bar represents a radial ring containing approximately 60 stars.

(1997) reported the kinematic PA of maximum rotation at 198° North through East. Here we adopt this value for the PA of the major axis (see Section 4.1).

2.2. Line-of-sight velocity sample

The bulk of the line-of-sight velocities come from the compilation by G00, who reported measurements for 1773 stars brighter than B magnitude 16.5 out to a radius of $17'$. Their data set includes earlier measurements by Peterson, Seitzer & Cudworth (1989), Dubath & Meylan (1994), Gebhardt et al. (1994, 1995, 1997) and Drukier et al. (1998), as well as 82 stars in the inner region measured using adaptive-optics-assisted spectroscopy (G00). In addition, line-of-sight velocities for 64 stars in the inner $4'$ were obtained with STIS on-board HST (van der Marel et al. 2002; Gerssen et al. 2002, 2003).

The expected number of non-members in this data set is very small. The cluster is very dense, so few interlopers are expected from chance superposition of field stars. The systemic line-of-sight velocity of M15 is $-107.5 \pm 0.2 \text{ km s}^{-1}$ (G00). With an internal velocity dispersion of about 12 km s^{-1} in the center, the cluster stars are well-separated in velocity from the foreground galactic disk. The bulk of the data is inside $4'$ and the median error of the line-of-sight velocities is 3.5 km s^{-1} . This is a significant fraction of the line-of-sight velocity dispersion, especially at larger radii.

2.3. Proper motions

M03 published proper motions for 1764 stars within 0.3 of the center of M15, derived from multi-epoch HST/WFPC2 imaging. The stars range in brightness between 14.0 and 18.3 mag. Of the 1764 stars only 703 stars brighter than B -magnitude 16.5 were kept and used in their analysis. We restrict ourselves to this sample of 703 stars.

M03 derived the proper motions in the classical way, by using a reference frame consisting of cluster stars, and then modeling the difference between the positions on the first and second epoch images in terms of a zero point difference, a scale change, a rotation, a tilt, and second-order distortion

corrections (e.g., Vasilevskis et al. 1979). The corresponding transformation equations were then solved using a least squares routine. As a result, the derived proper motions are not absolute, but may contain a residual global rotation. They also may be influenced by perspective rotation caused by the space motion of the cluster. We return to this in Section 3.

Figure 1 of M04 shows the histogram of all proper motions. The median error of these measurements is 0.12 mas yr^{-1} , corresponding to about 6 km s^{-1} at a distance of 10 kpc, with some errors as large as 0.50 mas yr^{-1} .

3. KINEMATICS

We use a Cartesian coordinate system (x', y', z') with z' along the line of sight and x' and y' in the plane of the sky aligned with the cluster such that the y' -axis is the photometric minor and rotation axis of the cluster. The kinematic measurements then give $v_{z'}$ for the line-of-sight velocities in km s^{-1} , and $\mu_{x'}$ and $\mu_{y'}$ for the proper motions in mas yr^{-1} . To convert $\mu_{x'}$ and $\mu_{y'}$ into $v_{x'}$ and $v_{y'}$ in km s^{-1} , we used $v_{x'} = 4.74D\mu_{x'}$ and $v_{y'} = 4.74D\mu_{y'}$, with D the distance in kpc.

The measurement errors in the line-of-sight velocities and in the proper motions need to be taken into account when analyzing the kinematics of M15. We do this by means of a maximum likelihood method, which corrects for each individual velocity error, and provides robust estimates of the mean velocities and velocity dispersions in spatial bins on the sky. The method is described in detail in Appendix A of V05.

3.1. Selection

Figure 1a shows the velocity dispersion along the line of sight, as a function of radius, for three different selections of stars. The blue curve is for all stars with velocity error smaller than 14 km s^{-1} , the black curve for those with errors smaller than 7 km s^{-1} , and the red curve for the stars with errors smaller than 5 km s^{-1} . Although we corrected the dispersion for the individual measurement errors, the curves do not all overlap, suggesting that the (larger) errors are not estimated very accurately. The curves converge once we exclude

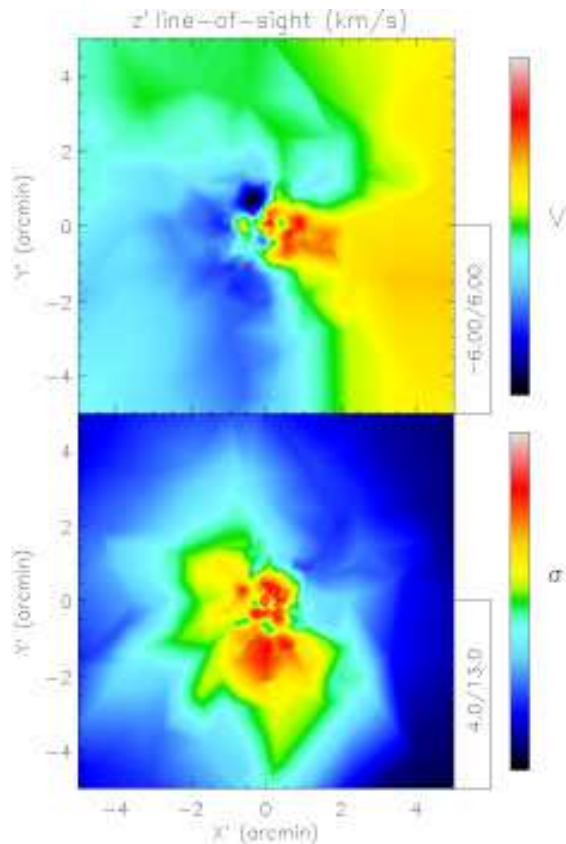


FIG. 2.— Smoothed line-of-sight mean velocity (top) and velocity dispersion field (bottom) for M15 in km s^{-1} .

the stars with errors larger than 7 km s^{-1} , so we restrict ourselves to this sample of 1546 stars. The corresponding profile varies between approximately 12 km s^{-1} in the center to 3 km s^{-1} at about $10'$ (cf. Figure 12 in G00).

Figure 1b shows the velocity dispersions of the proper motions in the x' and y' direction, respectively, as a function of radius, for three different selections of stars based on the measurement errors, corresponding to 21, 14 and 8 km s^{-1} for an assumed distance of 10 kpc. The radial range covered is only $0'.23$, and hence corresponds to the inner data points of Figure 1a. The profiles for the different error selections are consistent to within the errors of the dispersions. The dispersion profiles in the two orthogonal directions appear to differ and they are, in fact, inconsistent at the formal one sigma level. The overall proper motion dispersion is independent of the error selection. It is therefore not evident that a selection based on measurement error is justified, and we use all 703 proper motions.

Figures 2 and 3 show a smooth representation of the mean velocity and dispersion fields of the line-of-sight velocities and proper motions, respectively. The fields were adaptively smoothed by computing at each stellar position the kinematic moment for the nearest 100 neighbors using Gaussian weighting with distance from the central star. The Gaussian used for the weighting has the mean distance of the 100 stars as its dispersion. The resulting smooth kinematic maps correlate the different values at different points, but bring out the main features of the observed kinematics of M15.

The line-of-sight velocity maps show significant structure, including overall rotation (G00; and Section 5 below). The line-of-sight velocity dispersion shows the radial fall-off illustrated in Figure 1a. The contours of constant dispersion

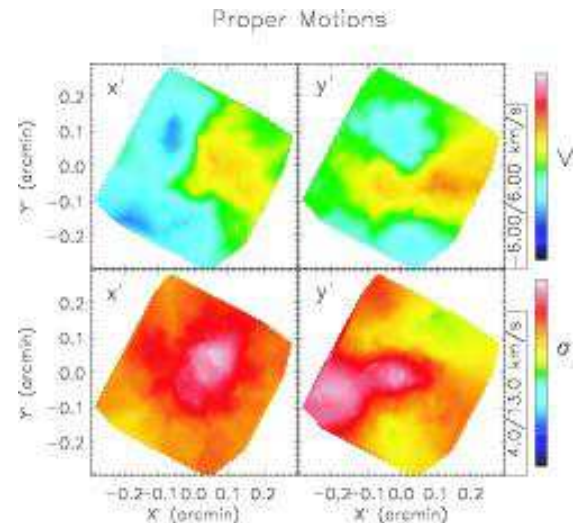


FIG. 3.— Smoothed kinematic velocity fields of the proper motions in km s^{-1} assuming a distance of 10 kpc. *Left*: kinematics in the x' -direction (parallel the major axis). *Right*: kinematics in the y' -direction (parallel the minor axis). *Top*: Velocity field. *Bottom*: Corresponding dispersion fields.

TABLE 1
SYSTEMIC PROPER MOTION OF M15

$\mu_{\alpha} \cos \delta$ (1)	μ_{δ} (2)	Reference (3)
-0.3 ± 1.0	-4.2 ± 1.0	Cudworth & Hanson (1993)
-1.0 ± 1.4	-10.2 ± 1.4	Geffert et al. (1993)
-0.1 ± 0.4	0.2 ± 0.3	Scholz et al. (1996)
-2.4 ± 1.0	-8.3 ± 1.0	Odenkirchen et al. (1997)
-0.95 ± 0.51	-5.63 ± 0.50	Dinescu et al. (1999)

NOTE.— Five determinations of the systemic motion of M15 on the plane of the sky. Cols (1) & (2): Systemic proper motion in α, δ in units of mas yr^{-1} . Col. (3): Reference.

are slightly elongated. The mean proper motion maps are difficult to interpret, because of the relatively large measurement errors. The dispersions in the proper motions are nearly constant over the small extent of the field (cf Figure 1b).

3.2. Perspective rotation

The observed motions contain a contribution from the perspective rotation caused by the space motion of M15. The systemic line-of-sight velocity is $-107.5 \pm 0.2 \text{ km s}^{-1}$ (Gebhardt et al. 1997), but the component of the space motion in the plane of the sky is not well-determined. Table 1 presents a summary of the reported space motions for M15.

Use of eq. (6) of V05 shows that any of the values in Table 1 result in contributions to the observed proper motions of at most $0.0025 \text{ mas yr}^{-1}$ at the edge of the small area where we have measurements. This is well below the measurement errors, and we therefore ignore it. The contribution to the observed line-of-sight velocities is $\pm 0.1 \text{ km s}^{-1}$ at $5'$ from the center if we use the Cudworth & Hanson (1993) value for the space motion, which is small enough that it can be ignored. If the more recent determinations by Odenkirchen et al. (1997) and Dinescu et al. (1999) are correct, then there would be a contribution of $\pm 0.8 \text{ km s}^{-1}$. This contribution is still not significant relative to the measurement errors and therefore we do not apply any correction for the perspective rotation. However, in this case perspective rotation would become important for studies of the kinematics near the tidal

radius ($21''.5$, Trager et al. 1995). If not corrected for, it would result in an apparent leveling-off of the line-of-sight velocity dispersion, as reported by Drukier et al. (1998).

3.3. Residual global rotation

It is possible to correct for the possible presence of residual global rotation in proper motion measurements of a globular cluster by using the line-of-sight velocities and the assumption of axisymmetry. V05 applied this method with success to ω Centauri. We follow the same approach for M15.

In an axisymmetric cluster, the following relation is valid between the mean motion $\langle\mu_{y'}\rangle$ and the mean line-of-sight velocity $\langle v_{z'}\rangle$ at any point (x', y') :

$$\langle v_{z'}\rangle = 4.74D \tan i \langle\mu_{y'}\rangle, \quad (1)$$

where $\langle v_{z'}\rangle$ is in units of km s^{-1} , D is the distance in kpc, i is the inclination of the cluster, and $\langle\mu_{y'}\rangle$ is in mas yr^{-1} (cf. Evans & de Zeeuw 1994). We computed the mean value $\langle\mu_{y'}\rangle$ in spatial bins on the plane of the sky, and similarly for $\langle v_{z'}\rangle$. We find a formal best-fit value which corresponds to an inclination of $59^\circ \pm 12^\circ$ at a distance of 10 ± 0.5 kpc.

If the proper motion measurements still contain an unknown amount of global rotation Ω (constant with radius), then the observed $\mu_{x'}$ and $\mu_{y'}$ should be replaced by

$$\mu_{x'} = \mu_{x'} + y' \Omega, \quad \mu_{y'} = \mu_{y'} - x' \Omega. \quad (2)$$

We stepped through a range of values of Ω and determined the value for which the scatter around the relation (1) was minimized. We find a weak minimum for Ω equal to -0.21 ± 0.22 $\text{mas (yr arcmin)}^{-1}$. The difference between the two cases is modest and changes the formal best-fit value of the inclination slightly to $54^\circ \pm 10^\circ$. We conclude that any effect of residual global rotation is below the measurement errors, and therefore we do not correct for it.

4. DYNAMICAL MODELS

We construct axisymmetric dynamical models of M15 by means of Schwarzschild's (1979) orbit superposition method, as implemented by Verolme et al. (2002). The inclusion of proper motion data is described in detail by V05, together with extensive tests designed to establish the accuracy with which the distance and internal structure can be recovered. These dynamical models are collisionless, which is not necessarily a valid assumption for a dense globular cluster such as M15.

We start by constructing a luminosity model (Section 4.1), and compute constraints from the observed kinematics binned into polar apertures (Section 4.2). In each aperture, we compare the mean velocities and velocity dispersions to the predictions of the dynamical model while varying the parameters to find a best-fit model. The model parameters are the inclination i , the distance D , the mass-to-light ratio (M/L) values in different radial bins and a central dark mass M_{dark} (Section 4.3). In Section 4.4, we obtain the best-fit models and we discuss the results in Sections 4.5, 4.6 and 4.7.

4.1. Luminosity model

We use the Noyola & Gebhardt (2005) V -band one-dimensional surface-brightness profile discussed in Section 2.1 as a basis for our mass model of M15. The profile extends to $15''$. We parameterized the profile with a multi-Gaussian expansion method (Monnet, Bacon & Emsellem 1992; Emsellem, Monnet & Bacon 1994) by means of the

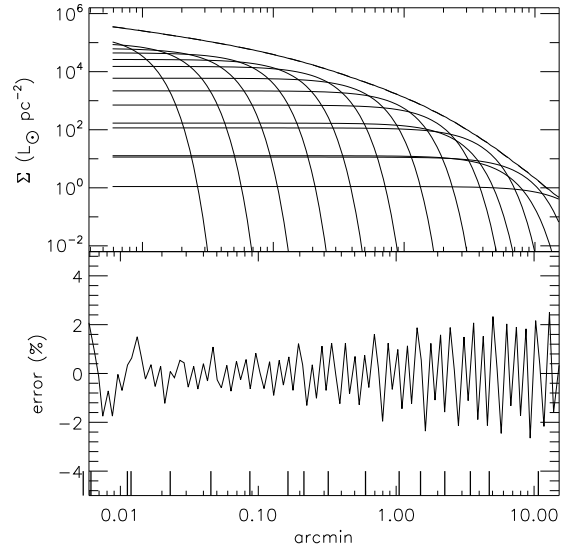


FIG. 4.— *Top*: Radial surface-brightness profile of M15 from Noyola & Gebhardt (2005) and the corresponding MGE best-fit model consisting of 14 Gaussians as a function of radius. Each individual Gaussian is shown as well. Left axis shows L_{\odot} per pc^2 . *Bottom*: The residual between the surface brightness and the MGE best-fit model. The profile is reproduced to within 3% over the entire radial range.

TABLE 2
MGE PARAMETERS FOR M15

# (1)	$\log I_{0,V} (L_{\odot} \text{pc}^{-2})$ (2)	$\log \sigma' (\text{arcmin})$ (3)	M/L (4)
1	5.306	-2.270	$5.0^{+7.0}_{-4.0}$
2	5.009	-1.923	1.9
3	4.822	-1.639	$1.0^{+0.9}_{-0.5}$
4	4.670	-1.343	1.1
5	4.442	-1.061	1.3
6	4.202	-0.784	$1.4^{+0.4}_{-0.4}$
7	3.795	-0.492	1.7
8	3.361	-0.223	2.0
9	2.871	0.022	2.3
10	2.250	0.177	$2.5^{+0.5}_{-0.5}$
11	2.084	0.353	2.5
12	1.127	0.538	2.5
13	1.080	0.675	2.5
14	0.066	1.031	2.5

NOTE. — The parameters of the 15 Gaussians from the MGE-fit to the V -band surface brightness profile of Noyola & Gebhardt (2005). Col. (1): number of Gaussian component. Col. (2): Central surface brightness of each Gaussian adjusted for the assumed ellipticity of $\epsilon = 0.05$. Col. (3) Dispersion along the major axis. Col. (4) Best-fit $M_{\odot}/L_{\odot,V}$ value for each Gaussian and associated error (See Section 4.6).

MGE fitting software developed by Cappellari (2002). Figure 4 shows the comparison between the observed profile and the MGE fit. Table 2 gives the numerical values of the Gaussians that comprise the MGE model. The fit is accurate to better than 3% at all radii. The smallest Gaussian in the MGE model has a sigma of $0''.23$ and the largest Gaussian has a sigma of $10''.7$. The mass outside the tidal radius is negligible.

We assume the photometric major axis is aligned with the axis of maximum rotation, as required for an axisymmetric model. We set the observed ellipticity of the Gaussian components to be $\epsilon = 0.05$, adjust the luminosity of the Gaussians

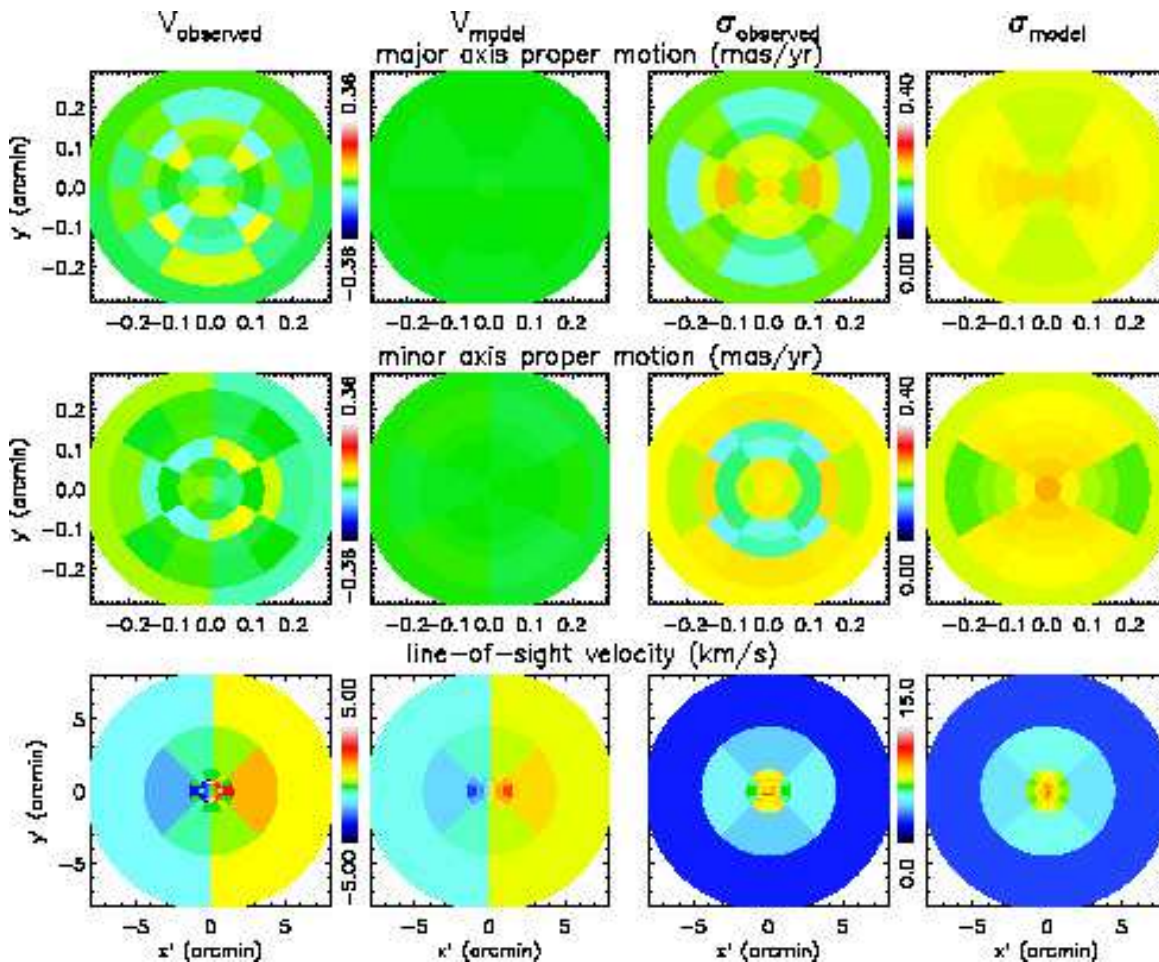


FIG. 5.— Observed mean velocity and velocity dispersion (first and third column) and the corresponding kinematics from the best-fit dynamical model with $D = 10.3$ kpc (second and fourth column). Top and middle row show the average kinematics of the proper motions in the x' and y' -direction and the bottom row shows the averaged kinematics of the line-of-sight velocities.

accordingly to conserve flux, and take the photometric major axis at $PA=198^\circ$ north through east (Gebhardt et al. 1997). The chosen ellipticity sets the minimum possible value of the inclination of M15 to be 25° , as otherwise the Gaussians cannot be projected to have the observed flattening. V05 showed that modest radial variations (or errors) in the ellipticity are not critical for the resulting best-fit models.

4.2. Aperture binning

We fit the dynamical models to the observed kinematic data, binned in apertures on the sky. Since the models are axisymmetric, we first reflect all the measurements to one quadrant, as described in V05, and then construct a grid of polar apertures. The apertures contain 50 stars per bin on average, except for the center where the bins contain only 10 stars. This allows an accurate measurement of the mean velocity and velocity dispersion (V05). We use different sets of apertures for the proper motions and the line-of-sight velocities. The 28 apertures and resulting $\langle v \rangle$ and σ for the line-of-sight data are shown in Figure 5, and given in Table 3. The line-of-sight apertures cover a large radial extent, from $7''$ to $10'$. The average velocity $\langle v \rangle$ and σ measurement error is 1.4 km s^{-1} and 1.0 km s^{-1} , respectively. The proper motion data is distributed over 13 apertures, also shown in Figure 5, with the corresponding values listed in Table 4. The average velocity $\langle v \rangle$ and σ measurement error is 0.04 mas yr^{-1} and 0.03 mas yr^{-1} respectively. The apertures extend to $18''.7$ from the center.

4.3. The parameters

M15 is a dense and old globular cluster in which substantial mass segregation has taken place (e.g., Dull et al. 1997) so that M/L is expected to vary with radius. Our Schwarzschild models therefore have not only the distance D and inclination i of M15 as free parameters, but must allow for a radial M/L variation.

In a constant M/L model, the gravitational potential is obtained by multiplying the luminosity of all the Gaussians in the MGE mass model (Table 2) with the same M/L value. To construct a mass model with a smooth radial M/L profile we varied the M/L of the individual Gaussians as this allows efficient calculation of the corresponding gravitational potential. However, to reduce the number of free parameters and to enforce a continuous profile we varied the first, third, sixth and tenth Gaussian and interpolated the other Gaussians logarithmically. The Gaussians ten through fourteen were given the same M/L value as Gaussian ten, because their individual M/L 's are not constrained well because only line-of-sight velocities are available at these radii. Finally, we include a central dark mass M_{dark} , represented by a point-mass potential. As a result, we have seven parameters: D , i , four for the M/L profile, and M_{dark} , for which we construct models.

4.4. Best-fit model

Our dynamical models each have 2058 orbits covering a radial range of $0''.16$ to $1923''$. Each model takes approxi-

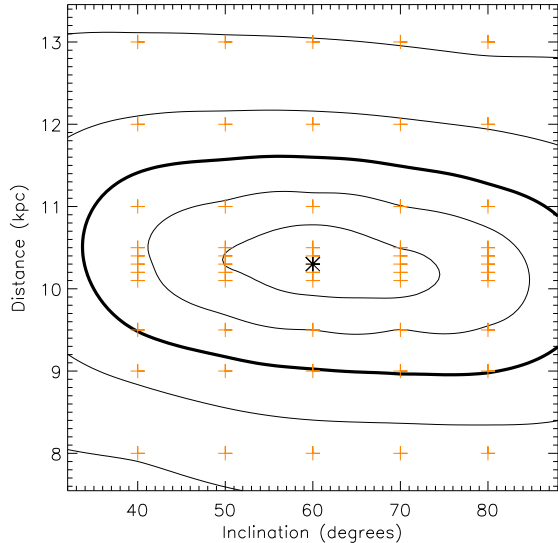


FIG. 6.— Marginalized χ^2 contour map of the models (crosses) varying inclination (horizontal axis) and distance (vertical). The three inner contours are drawn at formal 68.3%, 95.4% and 99.7% confidence levels for one degree of freedom. The subsequent contour corresponds to a factor two increase in $\Delta\chi^2$. The contours outside the models are extrapolated. The best-fit model at inclination 60° and 10.3 kpc is denoted with a black star. The inclination is not well constrained.

mately 40 minutes on an average 1.5Ghz desktop computer to complete. So a straightforward search of the parameters is impractical as this would require a minimum of $7^5 = 16807$ models. Therefore we first searched the three parameters D , i , M_{dark} to find their best-fit values. After that we searched M_{dark} and the four M/L parameters keeping D , i , fixed at their best-fit values. Finally we checked that we found the global minimum by doing a small search (7^3 models) through all the parameters.

The model that best fits the photometric and kinematic observations of M15 has a total of 275 constraints and a $\chi^2 = 88$. To determine the error on the parameters we will use $\Delta\chi^2 = \chi^2 - \chi^2_{min}$, where χ^2_{min} is the χ^2 of the best fitting model. We will use $\Delta\chi^2 = 3.53$ for the 68.3% confidence for one free parameter for D and i and $\Delta\chi^2 = 5.87$ for the 68.3% confidence for 5 free parameters for M_{dark} and the M/L profile. Since our reduced χ^2 is much smaller than one, our use of $\Delta\chi^2$ is conservative since we likely over-estimate our uncertainties.

The best-fit model has the following parameters $D = 10.3 \pm 0.4$ kpc, $i = 60 \pm 15$, $M_{dark} = 500^{+2500}_{-500} M_\odot$ and a radially varying M/L profile. The best-fit M/L values are tabulated in Table 2 and shown in Figures 7 and 8 with their formal error bars. The best-fit kinematics are shown in Figure 5. Due to the small number of stars in each aperture bin the scatter in the observed kinematics is large. The proper motion mean velocities are dominated by the errors. As a result, the mean proper motions of the best-fit model are very small. The overall rotation present in the line-of-sight velocities is fitted with the model. Also the observed dispersions are reproduced well.

4.5. Inclination and Distance

The $D \tan i$ fit of Section 3.3 gives an inclination of $59^\circ \pm 12^\circ$ at a distance of 10 kpc. The contours in Figure 6 show that the best-fitting inclination is $60^\circ \pm 15^\circ$ (68.3% confidence, one parameters), and as such the inclination is consistent with the $D \tan i$ prediction, although it is not constrained very well.

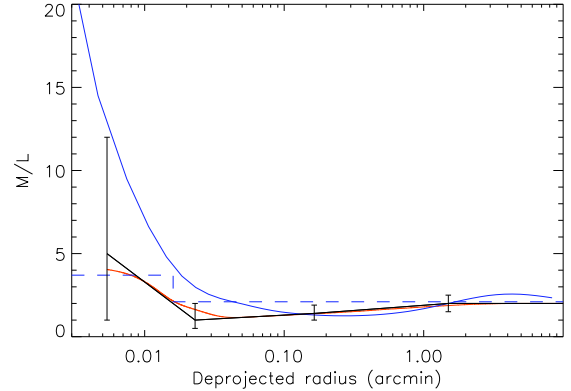


FIG. 7.— Radial M/L Profiles. *Black line*: Our best-fit V-band MGE M/L values and error bars signifying 68% confidence for five degrees of freedom. *Red line* Our best-fit deprojected M/L profile. *Blue solid line*: The deprojected M/L profile from Baumgardt (priv. comm.) *Blue dashed line*: Profile from Pasquali et al. See Section 4.6 and 4.7 for a discussion.

The dynamical distance estimate of 10.0 ± 0.5 kpc from M04 which assumes M15 is an isotropic sphere is very similar to our best-fit distance. Our (consistent) distance is slightly larger, because we allow our models the freedom to be flattened, and have not restricted the distribution function to be isotropic.

Our best-fit distance of 10.3 ± 0.4 kpc (68.3% confidence, one parameter) is in agreement with all other distance estimates: 10.4 ± 0.8 kpc by Durrel & Harris (1993), 10.3 kpc from the globular cluster catalog of Harris (1996), 9.5 ± 0.6 kpc by Silberman & Smith (1995), and the Fe II metallicity-scale distance 11.2 kpc by Kraft & Ivans (2003).

4.6. The M/L profile

Our best-fit M/L model profile is shown in black in Figure 7 with the formal error bars. The error bars in Figure 7 denote 68% confidence errors of the five parameter fit. Interpreting the error bars is difficult, since the error bars are a one-dimensional view of the five-dimensional parameter space. The M/L values (and their errors) at the different radii are strongly correlated, since they represent enclosed mass. The values are listed in Table 2, and can be used to convert the individual Gaussian luminosity profiles into density profiles. Summing these provides the density profile for M15. Division by the luminosity profile then gives a smooth M/L profile. This is shown in red.

Pasquali et al. (2004) find an $M_\odot/L_\odot = 2.1$ at $7'$ and an $M_\odot/L_\odot = 3.7$ in the center using a luminosity and mass function derived from NICMOS data. Their results agree with our M/L profile as shown in Figure 7 with a blue dashed line. Another independent measurement of the central M/L by Phinney (1993) using the acceleration of pulsars in M15 yield a lower limit of the M_\odot/L_\odot of 2.1 inside $0'.1$ and is consistent with our profile.

The blue curve in Figure 7 is the radial M/L profile of M15 from an N-body model constructed by Baumgardt (priv. comm.), which is rather similar to that of Dull et al. (2003). It has a central peak, caused by compact remnants, mostly massive white dwarfs. The total number of these remnants that survive the cluster evolution is difficult to estimate, as it depends on the fraction of neutron stars that is retained in the cluster potential after supernova explosion, which is believed to endow them with substantial kick velocities (Hansen & Phinney 1997; Pfahl, Rappaport & Podsiadlowski 2002).

The profile from Baumgardt is significantly different from our best-fit model inside $0'.6$. To be able to accurately de-

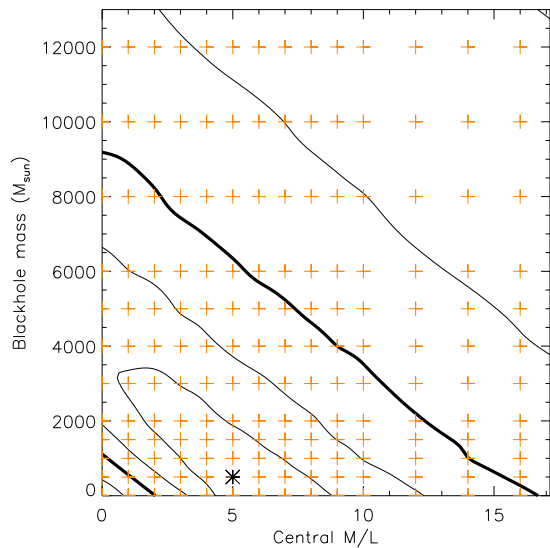


FIG. 8.— Marginalized χ^2 contour map of the models (crosses) varying the central M_{\odot}/L_{\odot} value (horizontal) and the dark central mass (M_{\odot} , vertical axis). The three inner contours are drawn at formal 68.3%, 95.4% and 99.7% confidence levels for three degrees of freedom. Subsequent contours correspond to a factor 2 increase in $\Delta\chi^2$. The best-fit model with a dark central mass of $500 M_{\odot}$ and a central M/L of $5 M_{\odot}/L_{\odot}$ is denoted with a black star. The correlation between the two parameters can clearly be seen, showing that the data primarily constrains the total central mass enclosed.

termine the difference we made models with the Baumgardt M/L profile instead of our own. These models did not include a dark central mass. The $\Delta\chi^2$ value we find for the best-fit model with Baumgardts M/L profile is outside our formal 99.9% confidence level of our best-fit model. The distance and inclination found by using the Baumgardt profile do not differ significantly from our best-fit values.

For completeness, we tried models with a constant M/L . The best-fit distance, inclination and central dark mass do not change significantly. The best-fit constant M/L found is $1.6 \pm 0.2 M_{\odot}/L_{\odot}$. This is the same as found by Gerssen et al. (2002) and consistent with $1.7 M_{\odot}/L_{\odot}$ found by Gebhardt (1997). The $\Delta\chi^2$ value found indicates that our constant M/L value is consistent with our M/L profile within 95.4% (two sigma) confidence levels.

Finally, the total mass of our best-fit model is $4.4 \times 10^5 M_{\odot}$. This is in agreement with $4.9 \times 10^5 M_{\odot}$ (Dull et al. 1997), $4.4 \times 10^5 M_{\odot}$ (M04) and $4.6 \times 10^5 M_{\odot}$ (G00). Our estimate of the total mass is sensitive to the largely unconstrained value of M/L outside of $2'$, as this region contains $\sim 40\%$ of the mass of the cluster.

4.7. Central dark mass

Previous studies by Peterson et al. (1989), Gebhardt et al. (1997) and Gerssen et al. (2002) have argued for an intermediate mass black hole (IMBH) of up to a few thousand M_{\odot} in M15. However M03 and Baumgardt et al. (2003) reported that they can construct N-body models for M15 which do not require an IMBH. For a detailed review of the history of this controversial subject, see M03 and van der Marel (2004).

Our formal best-fit value of the dark central mass is $500^{+2500}_{-500} M_{\odot}$ ($\Delta\chi^2 = 1$). This mass estimate agrees with all the earlier estimates of the IMBH from Gebhardt (1997) to Gerssen et al. (2002). Figure 8 shows that there is a degeneracy between the central M/L and dark central mass.

To be able to determine the inner structure, accurate information on the central region is critical as it is difficult to de-

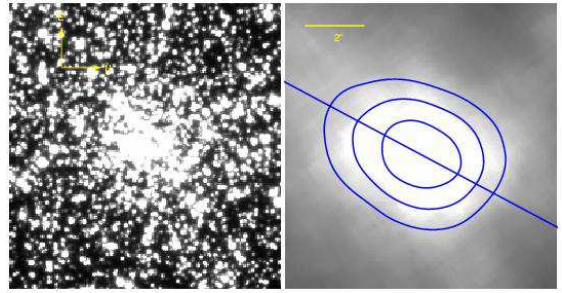


FIG. 9.— Images of the central region of M15, $9''$ on a side. The left image is a WFPC2/F336W exposure. The right image is heavily massaged; we have convolved the original image with a boxcar of 20 pixels in size. The blue curves are smoothed isophotes at $1''.5$, $2''.2$ and $2''.8$ major axis radius. The straight line is the best-fit position angle for the isophotal major axis.

termine what happens in the central part that is not covered by luminosity and kinematic data. The sphere of influence for a $1000 M_{\odot}$ black hole is $0''.5$. The inner luminosity data point that we used in this model is at $0''.35$ from the center and the closest star is $0''.4$ and $0''.25$ from the center for the line-of-sight and proper motion data set, respectively. This results in a degeneracy between the central M/L and dark central mass as is shown in Figure 8. As a result we are not able to determine the nature of the matter inside $\sim 1''$. By combining the mass of our best-fit mass model and the dark central mass we estimate that the total mass inside $1''.0$ arcsec (0.05 parsec, 10^4 AU at 10.3 kpc) is $3400 M_{\odot}$. This implies an extremely high central density of $7.4 \times 10^6 M_{\odot} \text{pc}^{-3}$.

To test the robustness of this density estimate we made models with a constant M/L (section 4.6) and a dark central mass. In this case we found the best-fit dark central mass to be $1000^{+4000}_{-1000} M_{\odot}$. The mass contained inside $1''.0$ in this model is comparable to that from our models with the best-fit M/L profile.

Guhathakurta et al. (1996) studied the cluster photometry of M15 using star counts. They detected 205 stars brighter than 20th magnitude in V-band inside $1''.0$. The typical mass of these post-main-sequence and turnoff stars is $0.75 M_{\odot}$, thus these stars account for $150 M_{\odot}$. Their data is not able to constrain the mass of fainter stars. But they give a rough (over) estimate and find that the total stellar mass is $4000 M_{\odot}$. When projected onto the sky our mass model gives a total mass of $5000 M_{\odot}$ in this region. This would mean that there is room for dark mass in the form of an IMBH with a mass in the order of $1000 M_{\odot}$. If mass segregation has indeed taken place, the stellar mass function used here might significantly overestimate the amount of low mass stars, and therefore lower the total stellar mass. This would allow for more dark matter inside $1''.0$.

5. A DECOUPLED CORE?

The maps of the velocity fields shown in Figure 3 display significant structure in the inner few arcseconds. If M15 is rotating, the plot of velocity against position angle for an annulus will show a sinusoidal variation (it is exactly sinusoidal for rotation on cylinders). Figure 10 shows the individual measurements in an annulus with inner and outer radii of $0''.03$ and $0''.06$ as a function of position angle on the plane of the sky (cf. Figure 14 of G00). There is little azimuthal variation in $v_{x'}$, but both $v_{y'}$ and $v_{z'}$ show a sinusoidal variation. Using relation (1), the line-of-sight velocity and y' proper motion suggest an inclination of $45 \pm 20^\circ$, consistent with our dynamical modeling result. Since the proper motions and radial velocities come from different dataset, the concordance of both results

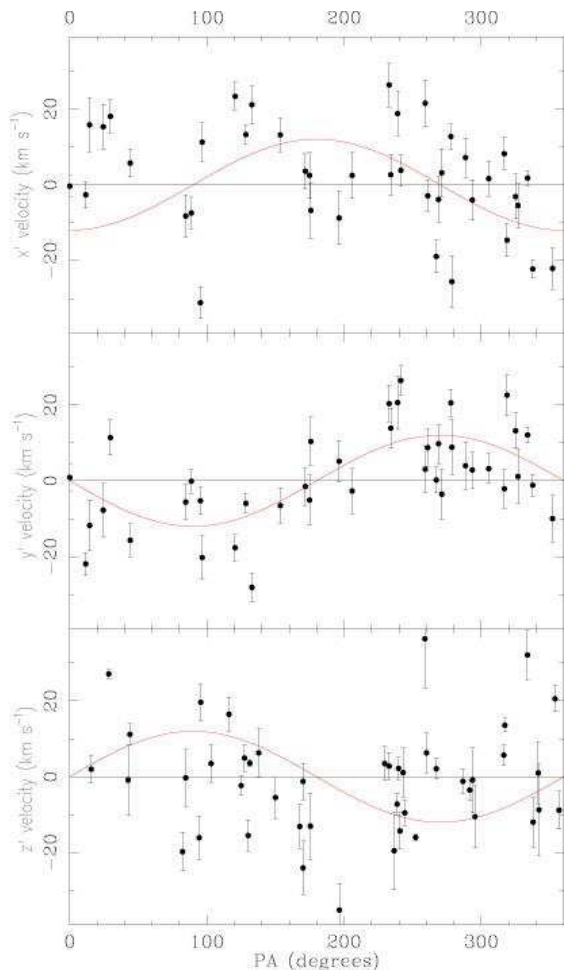


FIG. 10.— Velocity of stars versus position angle on the sky for each velocity component. The top is for the motion parallel to the major axis, the middle is along the minor axis, and the bottom is the line-of-sight motion. The line is the best fit profile with a three-parameter fit. We fit the position angle of the major axis, amplitude of the rotation along minor and line-of-sight axes, and amplitude along the major axis. The position angle of the maximum in the line-of-sight velocity corresponds to the isophotal major axis of the central structure in M15.

and individual significance of the rotation in each component strongly suggest that the central rotation in M15 is real. A simultaneous fit to the two kinematic data sets, subject to the constraint (1), sets the y' -amplitude to $11 \pm 1.5 \text{ km s}^{-1}$ and x' -amplitude to $7 \pm 1.5 \text{ km s}^{-1}$, at a PA of $270 \pm 10^\circ$.

Figure 9 shows the central region of M15 as observed with WFPC2/F336W. We have heavily smoothed the image on the right-hand side in order to measure any potential flattening. The image does show substantial flattening, which appears in a F555W image as well. The position angle of the major axis is not at either the kinematic PA nor at the isophotal PA of the major axis at large radius. We find a position angle of $\sim 120^\circ$ (North to East) for the light inside of $3''$. This PA is 30 degrees different from the kinematical PA as defined by the rotation seen in the core. Although this difference is significant given the uncertainty on the kinematically defined PA, the photometrically determined PA is subject to collections of bright stars and it is difficult to determine uncertainties for it. Thus, we are unable to determine whether the difference in the kinematic and photometric PA in the central region is significant.

It is tempting to identify this misaligned structure with the signature of an inspiraling binary IMBH, as described by

Mapelli et al. (2005). Their simulations of binary IMBH predict a small number of stars with high rotational velocities close to the black hole, and then a larger number of stars with aligned angular momentum (i.e., central rotation). However, we see no evidence for a small number of associated high velocity stars, which would be a direct signature in their scenario. We do though see ordered rotation. This rotation is not direct evidence for a binary black hole, but it does suggest an unexpected dynamical state for the central regions in M15. Since the relaxation time is very short in the center of M15 (around 10^7 years), rotation will be quickly removed by two-body interaction (Akiyama & Sugimoto 1989; Kim, Lee & Spurzem 2004). As discussed in Gebhardt et al. (2000), it is difficult to maintain such strong rotation in the central parts of M15. A binary IMBH does increase the central relaxation time (by lowering the stellar density) and offers a possible formation mechanism—and even explains the misalignment between the core and halo PA—but one would need stronger evidence in order to invoke such a scenario.

The misaligned core is inconsistent with our assumption of an axisymmetry dynamical model for M15, with major axis at PA of 198° . When we ignore the kinematic measurements inside $4''$ in the fitting procedure, we obtain the same distance and inclination.

6. DISCUSSION AND CONCLUSIONS

We studied the globular cluster M15 by fitting line-of-sight velocities, HST proper motions and surface brightness profiles with orbit-based axisymmetric dynamical models.

The observations used for the modeling consisted of a luminosity profile from Noyola & Gebhardt (2005), 1264 line-of-sight velocity measurements from G00 and a sample of 703 HST proper motions from M03. The line-of-sight data extends out to $7'$, while the proper motions cover the inner $0.25'$. The models provide a good fit to the observations and allow us to measure the distance and inclination of the cluster, the orbital structure, and the mass-to-light ratio M/L as a function of radius. We obtain a best-fit value for the inclination of $i = 60^\circ \pm 15$ and a dynamical distance of $D = 10.3 \pm 0.4 \text{ kpc}$, in good agreement with the canonical value.

Our best-fit model has a $500_{-500}^{+2500} M_\odot$ dark central mass and the M/L profile shown in Figure 7, which has a central peak and a minimum at $0.1'$. The overall shape of the profile resembles the shape expected for an expanded core globular cluster (Dull et al. 2003). The central M/L peak and the dark central mass together represent a mass of $3400 M_\odot$ inside the inner $1.0'$ (0.05 parsec at a distance of 10.3 kpc). This suggests that the center harbors a large amount of dark mass. We cannot distinguish the nature of the central mass concentration. It could be an IMBH or it could be large number of compact objects, or it could be a combination.

We found that a heavily smoothed image of M15 shows a flattened structure inside $4''$, with a different PA from the outer part of the cluster. The line-of-sight and proper motion data inside this radius can be fitted using relation (1). The fit gives a PA similar to that of the flattened structure and a rotational velocity of 10 km s^{-1} . This suggests the structure is real, and constitutes a fast-spinning decoupled core at the center of the cluster.

A significant improvement in the accuracy of the dynamical models for M15 is possible by increasing the accuracy of the proper motions and radial velocities. This appears possible with the ACS onboard HST, and with high-resolution spectrographs on 8m class tele-

TABLE 3
KINEMATICS OF THE PROPER MOTIONS IN POLAR APERTURES

#	n_*	r_0	θ_0	Δr	$\Delta\theta$	$V_{x'}$	$\Delta V_{x'}$	$\sigma_{x'}$	$\Delta\sigma_{x'}$	$V_{y'}$	$\Delta V_{y'}$	$\sigma_{y'}$	$\Delta\sigma_{y'}$
(1)	(2)	(3)	(4)	(5)	(6)	(7)	(8)	(9)	(10)	(11)	(12)	(13)	(14)
1	50	0.021	0.785	0.033	1.571	-0.04	0.04	0.25	0.03	-0.02	0.04	0.24	0.04
2	51	0.060	0.393	0.046	0.785	-0.02	0.04	0.21	0.02	-0.02	0.04	0.22	0.03
3	54	0.060	1.178	0.046	0.785	-0.04	0.03	0.23	0.02	-0.01	0.04	0.25	0.03
4	54	0.108	0.262	0.050	0.524	0.01	0.04	0.28	0.02	-0.00	0.03	0.19	0.03
5	54	0.108	0.785	0.050	0.524	0.06	0.04	0.22	0.03	0.07	0.03	0.19	0.03
6	63	0.108	1.309	0.050	0.524	0.02	0.03	0.23	0.03	0.04	0.03	0.17	0.03
7	45	0.154	0.262	0.043	0.524	0.02	0.04	0.22	0.02	0.04	0.04	0.26	0.03
8	48	0.154	0.785	0.043	0.524	-0.06	0.03	0.21	0.03	-0.01	0.03	0.15	0.03
9	61	0.154	1.309	0.043	0.524	0.03	0.03	0.19	0.02	-0.02	0.02	0.19	0.02
10	56	0.214	0.262	0.077	0.524	-0.02	0.02	0.15	0.03	-0.02	0.03	0.22	0.02
11	58	0.214	0.785	0.077	0.524	0.02	0.03	0.21	0.03	0.00	0.03	0.25	0.03
12	62	0.214	1.309	0.077	0.524	-0.05	0.03	0.18	0.02	-0.01	0.03	0.25	0.03
13	47	0.279	0.785	0.053	1.571	0.01	0.04	0.21	0.02	-0.03	0.04	0.24	0.02

NOTE. — The mean velocity and velocity dispersion of the proper motion observations calculated in polar apertures on the plane of the sky. Per row the information per aperture is given. The first column labels the aperture and the second column gives the number of stars n_* that fall in the aperture. Columns 3–6 list the polar coordinates r (in arcmin) and the angle θ (in degrees) of the centroid of the aperture and the corresponding widths Δr (in arcmin) and $\Delta\theta$ (in degrees). The remaining columns present the average proper motion kinematics in units of mas yr^{-1} . The mean velocity V with error ΔV and velocity dispersion σ with error $\Delta\sigma$ are given in columns 7–10 for the proper motion component in the x' -direction and in columns 11–14 for the proper motion component in the y' -direction.

scopes.

KG acknowledges support from NASA through grant number HST-AR-09542 from the Space Telescope Science

Institute, which is operated by AURA, Inc., under NASA contract NAS5–26555 and NSF CAREER grant AST-0349095. TdZ gratefully records the warm hospitality of Neal Evans and Leslie Geballe during part of this work.

REFERENCES

- Akiyama, K. & Sugimoto, D. 1989, PASJ, 41, 991
Baumgardt H., Hut P., Makino J., McMillan S., Portegies Zwart S., 2003, ApJ, 582, L21
Binney J.J., Tremaine S.D., 1987, Galactic Dynamics, Princeton University Press
Cappellari, M. 2002, MNRAS, 333, 400
Cudworth K.M., 1979, ApJ, 420
Cudworth K.M., Hanson R.B., 1993, AJ, 105, 168
Dinescu D.I., Girard T.M., van Altena W.F., 1999, AJ, 117, 1792
Drukier G.A., Slavin S.D., Cohn H.N., Lugger P.D., Berington R.C., Murphy B.W., Seitzer P.O., 1998, AJ, 115, 708
Dubath P., Meylan G., 1994, AA, 290, 104
Dull J.D., Cohn H.N., Lugger P.M., Murphy B.W., Seitzer P.O., Callanan P.J., Rutten R.G.M., Charles P.A., 1997, ApJ, 481, 267
Dull J.D., Cohn H.N., Lugger P.M., Murphy B.W., Seitzer P.O., Callanan P.J., Rutten R.G.M., Charles P.A., 2003, ApJ, 585, 598
Durrell P.R., Harris W.E., 1993, AJ, 105, 1420
Evans N.W., de Zeeuw P.T., 1994, MNRAS, 271, 202
Gebhardt K., Pryor C., Williams T.B., Hesser J.E., 1994, AJ, 107, 2067
Gebhardt K., Pryor C., Williams T.B., Hesser J.E., 1995, AJ, 110, 1699
Gebhardt K., Pryor C., Williams T.B., Hesser J.E., Stetson P.B., 1997, AJ, 113, 1026
Gebhardt K., Pryor C., O'Connell D., Williams T., 2000, AJ, 119, 1268 (G00)
Geffert, M., Colin J., La Campion J.-F., Odenkirchen M., 1993, AJ, 106, 168
Gerssen J., van der Marel R.P., Gebhardt K., Guhathakurta P., Peterson R., Pryor C., 2002, AJ, 124, 3270
Gerssen J., van der Marel R.P., Gebhardt K., Guhathakurta P., Peterson R., Pryor C., 2003, AJ, 125, 376
Guhathakurta P., Yanny B., Schneider D.P., Bahcall J.N., 1996, AJ, 111, 267
Hansen B.M.S., Phinney E.S., 1997, MNRAS, 291, 569
Harris, W. E. 1996, AJ, 112, 1487
Kim, E., Lee, H.M., & Spuzem, R. 2004, MNRAS, 351, 220
Kraft R.P., Ivans I., 2003, PASP, 115, 143
Lauer T.R., et al., 1991, ApJ, 369, L45
Mappelli M., Colpi M., Possenti A., Sigurdsson S., 2005, astro-ph/0506405
McNamara B.J., Harrison T.E., Anderson J., 2003, ApJ, 595, 187 (M03)
McNamara B.J., Harrison T.E., Baumgardt H., 2004, ApJ, 602, 264 (M04)
Monnet, G., Bacon, R., & Emsellem, E. 1992, A&A, 253, 366
Monnet, G. 1994, Astronomy with the CFHT Adaptive Optics Bonnette, 110
Noyola E., Gebhardt K., 2005, ApJ, submitted
Odenkirchen M., Brosche P., Geffert M., Tcholke H.-J., 1997, NewA, 2, 477
Pasquali A., De Marchi G., Pulone L., Brigas M.S., 2004, AA, 428, 469
Peterson R.C., Seitzer P.O., Cudworth K.M., 1989, ApJ, 347, 251
Pfafl, E., Rappaport, S., & Podsiadlowski, P. 2002, ApJ, 573, 283
Phinney E.S., 1993, Structure and Dynamics of Globular Clusters, eds S.G. Djorgovski & G. Meylan, ASP Conf. Ser., 50, 141
Scholz R.-D., Odenkirchen M., Hirte S., Irwin M.J., Bornger F., Ziener R., 1996, MNRAS, 278, 251
Silbermann, N. A., & Smith, H. A. 1995, AJ, 110, 704
Sosin C., King I.R., 1997, AJ, 113, 1328
Trager S.C., King I.R., Djorgovski S., 1995, AJ, 110, 704
van der Marel R.P., Gerssen J., Guhathakurta P., Peterson R.C., Gebhardt K., 2002, AJ, 124, 3255
Vasilevskis S., van Leeuwen F., Nicholson W., Murray C.A., 1979, A&AS, 37, 333
van de Ven G., van den Bosch R.C.E., Verolme E.K., de Zeeuw P.T., 2005, A&A, 2006, 445, 513 (V05)
Verolme E.K., Cappellari M., Copin Y., van der Marel R.P., Bacon R., Bureau M., Davies R.L., Miller B.M., de Zeeuw P.T., 2002, MNRAS, 335, 517
White, R. E., & Shawl, S. J. 1987, ApJ, 317, 246

TABLE 4
KINEMATICS OF THE LINE-OF-SIGHT VELOCITIES IN POLAR APERTURES

# (1)	n_* (2)	r_0 (3)	θ_0 (4)	Δr (5)	$\Delta\theta$ (6)	$V_{z'}$ (7)	$\Delta V_{z'}$ (8)	$\sigma_{z'}$ (9)	$\Delta\sigma_{z'}$ (10)
1	10	0.015	0.785	0.022	1.571	0.6	3.8	10.8	2.6
2	10	0.030	0.785	0.008	1.571	1.0	4.1	10.4	2.5
3	10	0.040	0.785	0.011	1.571	-0.7	4.8	13.0	3.8
4	10	0.049	0.785	0.007	1.571	-8.9	4.2	11.2	2.2
5	62	0.103	0.393	0.102	0.785	0.2	1.6	11.3	1.1
6	56	0.103	1.178	0.102	0.785	1.2	1.8	12.8	1.4
7	55	0.214	0.262	0.120	0.524	1.4	1.4	9.4	0.9
8	63	0.214	0.785	0.120	0.524	2.3	1.3	9.3	1.0
9	52	0.214	1.309	0.120	0.524	3.2	1.4	9.4	0.9
10	63	0.366	0.196	0.184	0.393	0.6	1.4	10.3	1.0
11	63	0.366	0.589	0.184	0.393	0.5	1.4	10.3	1.0
12	54	0.366	0.982	0.184	0.393	1.8	1.9	12.3	1.1
13	70	0.366	1.374	0.184	0.393	1.7	1.2	10.2	0.9
14	53	0.553	0.196	0.190	0.393	0.7	1.5	10.2	1.2
15	57	0.553	0.589	0.190	0.393	3.6	1.5	9.8	0.8
16	63	0.553	0.982	0.190	0.393	2.5	1.2	9.6	0.8
17	60	0.553	1.374	0.190	0.393	0.7	1.3	9.5	0.8
18	61	0.791	0.196	0.286	0.393	2.7	1.3	9.0	0.8
19	69	0.791	0.589	0.286	0.393	2.5	1.2	9.3	0.8
20	78	0.791	0.982	0.286	0.393	2.9	1.1	8.5	1.0
21	48	0.791	1.374	0.286	0.393	3.4	1.5	9.9	2.1
22	68	1.165	0.196	0.462	0.393	3.4	1.0	7.8	0.8
23	49	1.165	0.589	0.462	0.393	1.0	1.3	8.0	1.2
24	66	1.165	0.982	0.462	0.393	0.6	1.1	8.5	1.4
25	62	1.165	1.374	0.462	0.393	1.2	1.2	9.1	2.0
26	60	2.560	0.393	2.329	0.785	1.8	0.8	6.5	0.7
27	66	2.560	1.178	2.329	0.785	0.4	0.9	6.7	1.0
28	60	5.306	0.785	3.163	1.571	1.5	0.6	3.9	0.4

NOTE. — The mean velocity and velocity dispersion calculated in polar apertures on the plane of sky from the line-of-sight velocity observations. Columns 1–6 are as in Table 3 and the remaining columns present the average line-of-sight kinematics in km s^{-1} .